

RESEARCH ARTICLE

Microscopic multifrequency MR elastography for mapping viscoelasticity in zebrafish

Jakob Ernst Luis Jordan¹  | Gergely Bertalan¹ | Tom Meyer¹  |
 Heiko Tzschätzsch¹  | Anton Gauert^{2,3}  | Luca Bramè^{2,3} | Helge Herthum⁴  |
 Yasmine Safraou¹ | Leif Schröder⁵  | Jürgen Braun⁴  | Anja I. H. Hagemann²  |
 Ingolf Sack¹  

¹Department of Radiology, Charité–Universitätsmedizin Berlin, Berlin, Germany

²Department of Hematology/Oncology, Charité–Universitätsmedizin Berlin, Berlin, Germany

³German Cancer Consortium (DKTK), German Cancer Research Center (DKFZ), Heidelberg, Germany

⁴Institute of Medical Informatics, Charité–Universitätsmedizin Berlin, Berlin, Germany

⁵Molecular Imaging, Leibniz-Forschungsinstitut für Molekulare Pharmakologie (FMP), Berlin, Germany

Correspondence

Ingolf Sack, Department of Radiology,
Charité–Universitätsmedizin Berlin,
Charitéplatz 1, 10117 Berlin, Germany.
Email: Ingolf.sack@charite.de

Funding information

Deutsche Forschungsgemeinschaft,
Grant/Award Number: BIOQIC, CRC
Matrix in Vision, GRK2260, SFB1340 and
Sa901/17-2

Purpose: The zebrafish (*Danio rerio*) has become an important animal model in a wide range of biomedical research disciplines. Growing awareness of the role of biomechanical properties in tumor progression and neuronal development has led to an increasing interest in the noninvasive mapping of the viscoelastic properties of zebrafish by elastography methods applicable to bulky and non-translucent tissues.

Methods: Microscopic multifrequency MR elastography is introduced for mapping shear wave speed (SWS) and loss angle (φ) as markers of stiffness and viscosity of muscle, brain, and neuroblastoma tumors in postmortem zebrafish with 60 μm in-plane resolution. Experiments were performed in a 7 Tesla MR scanner at 1, 1.2, and 1.4 kHz driving frequencies.

Results: Detailed zebrafish viscoelasticity maps revealed that the midbrain region (SWS = 3.1 ± 0.7 m/s, $\varphi = 1.2 \pm 0.3$ radian [rad]) was stiffer and less viscous than telencephalon (SWS = 2.6 ± 0.5 m/s, $\varphi = 1.4 \pm 0.2$ rad) and optic tectum (SWS = 2.6 ± 0.5 m/s, $\varphi = 1.3 \pm 0.4$ rad), whereas the cerebellum (SWS = 2.9 ± 0.6 m/s, $\varphi = 0.9 \pm 0.4$ rad) was stiffer but less viscous than both (all $p < .05$). Overall, brain tissue (SWS = 2.9 ± 0.4 m/s, $\varphi = 1.2 \pm 0.2$ rad) had similar stiffness but lower viscosity values than muscle tissue (SWS = 2.9 ± 0.5 m/s, $\varphi = 1.4 \pm 0.2$ rad), whereas neuroblastoma (SWS = 2.4 ± 0.3 m/s, $\varphi = 0.7 \pm 0.1$ rad, all $p < .05$) was the softest and least viscous tissue.

Conclusion: Microscopic multifrequency MR elastography-generated maps of zebrafish show many details of viscoelasticity and resolve tissue regions, of great

This is an open access article under the terms of the Creative Commons Attribution-NonCommercial-NoDerivs License, which permits use and distribution in any medium, provided the original work is properly cited, the use is non-commercial and no modifications or adaptations are made.

© 2021 The Authors. *Magnetic Resonance in Medicine* published by Wiley Periodicals LLC on behalf of International Society for Magnetic Resonance in Medicine.

interest in neuromechanical and oncological research and for which our study provides first reference values.

KEYWORDS

MR elastography, neuroblastoma, stiffness, tumors, viscoelasticity, zebrafish

1 | INTRODUCTION

Over the past 4 decades, zebrafish have emerged as a versatile animal model^{1,2} for a wide range of research areas, including embryology,³ oncology,⁴ tissue regeneration,⁵ and toxicology.⁶ The zebrafish genome is remarkably similar to that of humans: 70% of its genes are homologous to the human genome, and 82% of genes associated with human diseases have also been found in zebrafish.⁷ In addition, the optical transparency during embryonic development and in some adult genetically modified zebrafish lines, high fecundity, rapid growth rate, and comparative ease of husbandry make zebrafish an attractive animal model for biomedical research. Due to its early transparency, the accessibility of the offspring for tissue manipulations, and the diverse options of genetic manipulation, optical microscopy up to subcellular levels presents the most common method of investigation in the zebrafish.^{4,8,9} Combined with genetic analyses even on a single cell level, the zebrafish provides an optimal tool for tissue fate mapping in vivo.^{10,11} Mapping of the biophysical properties of zebrafish, however, is still in its infancy. Stiffness values of some zebrafish tissues have been reported based on invasively administered beads¹² and local optical tweezer experiments,¹³ which do not provide spatially resolved maps. Preliminary elastography data from zebrafish were obtained using ultrasonic elastography, but only averaged stiffness values for the central region of the fish were reported.¹⁴

MR elastography (MRE) is a versatile method that allows the noninvasive and 3D, spatially resolved mapping of viscoelasticity parameters in soft tissues for clinical diagnosis,¹⁵ and biomedical research.^{16–20} High-field MRE in small animal scanners has been applied to a wide variety of animal models, including Yucatan mini-pigs,²¹ ferrets,²² mice,^{18,23–25} rats,^{26,27} and frog oocytes.²⁸ In small animal models, MRE can provide maps of viscoelasticity with a pixel size on the order of 180 μm .²⁴ Higher resolution wave-encoding with 34 μm pixel size was demonstrated in gel phantoms and frog oocytes but without mapping the heterogeneity of viscoelastic parameters.²⁸ Given the very complex anatomy of zebrafish, high-resolution wave-encoding and viscoelasticity mapping based on multifrequency inversion methods^{29,30} may promote MRE in zebrafish for biomedical research.

To this end, we developed a multifrequency MRE technique for a 7 Tesla small-animal MRI scanner, a cylindrical actuator in which a zebrafish can be placed, a piezoelectrical actuator that induced predominantly cylindrical waves, and a spin-echo MRE sequence. Together, these provide an in-plane resolution of 60 μm for depicting details of zebrafish mechanical anatomy. The relevance of this method for oncological research will be demonstrated in wild-type and a transgenic neuroblastoma zebrafish model (Tg(dbh:MYCN;dbh:EGFP). The transgenic fish develop neuroblastoma tumors together with a fluorescence reporter mainly in the interrenal gland orthologues to the human adrenal medulla.³¹ Subregional analysis was performed to provide first reference values of stiffness in terms of shear wave speed (SWS in m/s) and viscosity in terms of loss angle of complex shear modulus (φ in radians) of the zebrafish brain, neuroblastoma tumor, and muscle tissue.

Our study has 3 objectives: (1) demonstrate the feasibility of MRE in zebrafish, (2) provide initial reference values for the viscoelastic properties of zebrafish muscles and brains, and (3) outline the prospect of using zebrafish as a model for biomechanically oriented oncology research. To this end, we first used a soft-viscous phantom, which was previously characterized by tabletop MRE to validate our sequence and inversion technique. We then studied both wild-type and transgenic zebrafish using high-field MRE. In a final step, we performed a histopathological examination in comparison with the heterogeneities visible in MRE maps.

2 | METHODS

2.1 | Phantom

To test the setup and to determine optimal image resolution as well as SNR, we produced a simple ultrasound gel (Gello GmbH Geltechnik, Germany) phantom. The phantom consists of ultrasound gel packed into a glass cylinder of 4 mm inner diameter, analogous to the one used in the animal experiment. Both ends of the glass cylinder were sealed off with rubber plugs (1.5 mm thickness). Ultrasound gel provides a good MRI signal (with T_1/T_2 relaxation times of 2600 ± 50 ms/ 42 ± 2 ms at 7 Tesla) and

transmits shear waves well. Its homogeneity also allows the use of global fits to determine SWS and φ values instead of the more error prone inversion algorithms needed for heterogeneous media. To optimize MRE image resolution based on ground truth values, we predetermined the viscoelastic parameters of the phantom over a wide frequency range from 200 to 1400 Hz using compact tabletop MRE and Bessel fitting of wave data.³² This method was used previously as reference method for soft gel analysis in the desired frequency range.^{24,33,34}

2.2 | Animals

Animals used in this study were kept under controlled conditions at the Pediatric Department of Oncology/Hematology and Stem Cell Transplantation, Charité University Hospital, Berlin, Germany, under the licenses ZH76 and G0325/19 approved by the local animal ethics committee (Landesamt für Gesundheit und Soziales, Berlin, Germany) (G0325/19) and was conducted in accordance with the European Community Council Directive of November 24, 1986 (86/609/EEC). A total of 22 adult wild type zebrafish (Tüpfel Long Fin) and 18 transgenic zebrafish (Tg(dbh:MYCN;dbh:EGFP) were investigated.³¹ The final groups consisted of 15 wild type fish (median age: 19 months, mean age: 14 months, range: 2 to 24 months) and 11 MYCN-transgenic fish (median age: 23 months, mean age 14 months, range: 6 to 25 months) due to technical failures (oversized: 2 wild type, 5 transgenic fish; incorrect imaging parameter settings: 3 wild type, 1 transgenic fish; insufficient shear wave amplitudes: 2 wild type, 1 transgenic fish). Before MRE, the fish were euthanized by hypothermal shock, as suggested by Wallace et al.³⁵ For MRI and MRE, the zebrafish were placed inside a glass cylinder of 4 mm inner diameter and embedded in ultrasound gel (Gello GmbH Geltechnik, Germany) to minimize tissue-air interfaces and susceptibility artifacts. Shear waves propagated into the fish by direct contact with the glass wall and through the ultrasound gel. The front end of the glass tube was sealed with a rubber plug (1.5 mm thickness).

2.3 | MRE actuator

Shear waves were induced through the walls of a cylindrical glass tube on which an air-cooled, nonmagnetic, piezoelectric actuator (ATA 200, Cedrat Technologies, France) was mounted. The main vibration direction was parallel to the cylinder axis to ensure that cylindrical shear waves with single polarization direction were predominantly

excited while compression waves were not excited or minimized by this geometry. This setup was designed to be similar to the vertical actuator of the MRE tabletop device but to allow excitation of waves in a horizontal orientation.³² The experimental setup is shown in Figure 1A. The actuator was driven by a function generator (CGC Instruments, Chemnitz, Germany) synchronized with the clock of the MRI scanner to avoid any latency between MRI and function generator while continuously vibrating the sample. Three vibration frequencies of 1000, 1200, and 1400 Hz were induced in consecutive experiments. All experiments were performed at $23 \pm 0.5^\circ\text{C}$.

2.4 | MRE image acquisition

All experiments were performed in a 7 Telsa preclinical MRI scanner (Bruker Biospec, Germany) equipped with a 5-mm bore, transverse electromagnetic, quadrature volume-resonator coil (Rapid Biomedical, Germany) shown in Figure 1. The MRE sequence was implemented using ParaVision 6.0.1 based on an existing spin-echo sequence that was sensitized to motion by including motion-encoding gradients of the same frequency, as used for mechanical vibrations. Motion-encoding gradients direction was along the main axis of the glass cylinder so that the predominant component of the cylindrical waves was encoded. Four dynamics of the wave cycle, evenly spaced over 1 vibration period, were encoded using a TE of 38 ms and a TR of 3000 ms. The motion-encoding gradients amplitude was 392 mT/m. Numbers of motion-encoding gradients periods were 14, 17, and 19, corresponding to 1000, 1200, and 1400 Hz vibration frequencies, respectively. Although this frequency range is too limited for analysis of viscoelastic dispersion in zebrafish tissue, previous work has shown that even minimal variation of excitation frequency enhances the stability of the inverse problems solution for the reconstruction of MRE maps using our k-MDEV (multifrequency dual elasto-visco) algorithm.^{36,37} For testing spatial resolution and SNR using the ultrasound gel phantom, matrix sizes of 100×100 , 67×67 , 50×50 , and 40×40 were used with a $4 \times 4 \text{ mm}^2$ FOV, resulting in in-plane pixel sizes of $40 \times 40 \mu\text{m}^2$, $60 \times 60 \mu\text{m}^2$, $80 \times 80 \mu\text{m}^2$, and $100 \times 100 \mu\text{m}^2$, respectively. Based on the results of the phantom experiment, we used the following parameters to measure the fish: 8 axial slices of 600 μm thickness, 67×67 matrix size, $4 \times 4 \text{ mm}^2$ FOV, and an in-plane resolution of $60 \times 60 \mu\text{m}^2$. The total acquisition time per frequency was approximately 16 min, and each fish was sampled from snout to swim bladder.

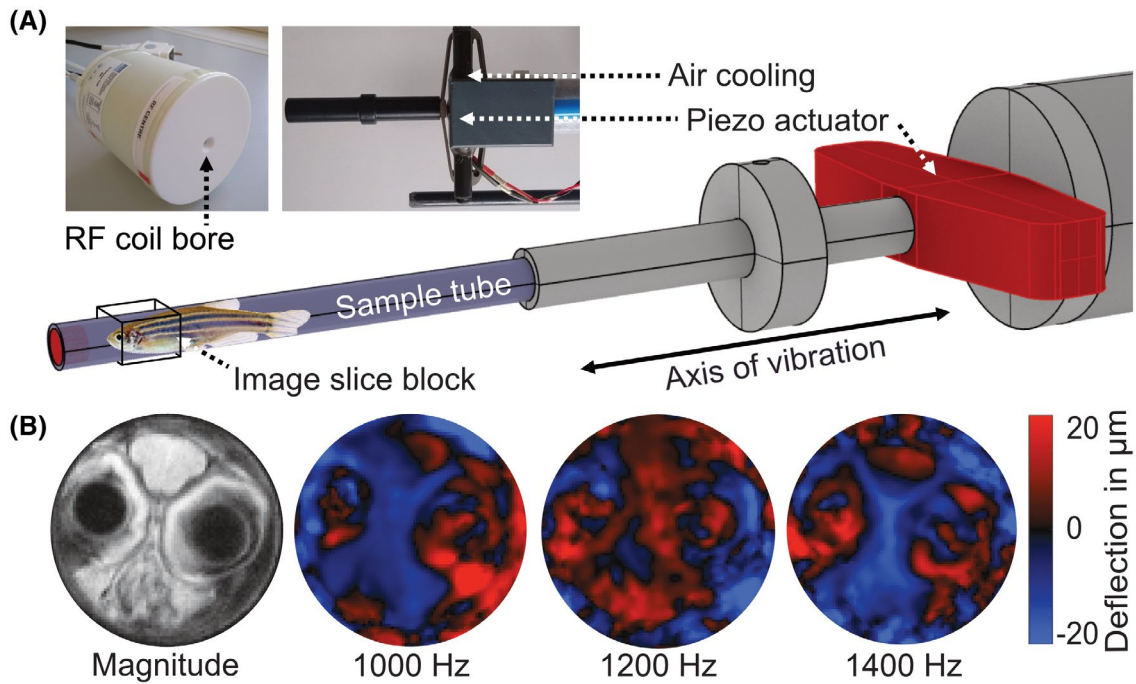


FIGURE 1 Setup for MRE of zebrafish in a 7T preclinical MRI scanner. (A) A piezoelectric actuation unit, shown in red, generates harmonic oscillations synchronized to the MRE sequence. The principal vibration direction is along the cylinder axis, which results in predominantly cylindrical waves. The box demarcates the area covered by the imaging slice slab. The custom volume resonator coil is also shown. (B) MRE magnitude image (grayscale) and wave images of different frequencies (color scale) showing the through-plane wave component, which was encoded by the sequence. MRE, MR elastography; T, tesla

2.5 | MRE data processing

After phase unwrapping and Fourier transformation across the 4 time steps over a wave cycle, the resulting complex-valued wave images at fundamental frequency. Examples shown in Figure 1B were reconstructed to maps of loss angle of complex shear modulus (φ in radian) using multifrequency dual elasto-visco (MDEV) inversion²⁹ and SWS using wave-number (k)-MDEV inversion.³⁰ The spatial bandpass filter of k -MDEV was adapted to the small field of view and minor impact of compression waves with our cylindrical actuator using a Butterworth filter of seventh order with 250/m threshold for the high pass. To facilitate comparison of values with the literature, we also tabulated shear stiffness in terms of the magnitude shear modulus $|G^*|$ assuming a material density ρ of 1000 kg/m³¹⁶:

$$|G^*| = \frac{SWS^2 \rho (1 + \cos \varphi)}{2}. \quad (1)$$

In ultrasound gel, SWS ground truth was determined by fitting Bessel functions as described previously.^{32,38,39} We consider Bessel function analysis of cylindrical waves as ground truth because it provides analytical solutions to the inverse problem in homogeneous media without artifact due to the dispersion-by-inversion bias.³⁸ Wave displacement SNR was

derived using the blind noise estimation method proposed by Donoho et al.⁴⁰ This method defines SNR as normalized log ratio of signal and median absolute deviation of the finest band of wavelet coefficients. The wavelet coefficients are calculated using Farras nearly symmetric filters.⁴¹ Both signal and noise are calculated only for regions of interest (ROI). Wavelet analysis is well suited for the differentiation of spatial frequencies of harmonic waves and noise in MRE, as shown previously.⁴² The method is implemented on an open access server for MRE data analysis (<https://bioic-apps.charite.de>).

In zebrafish, φ and SWS maps were analyzed for sub-regional differences by manually delineating ROIs in the magnitude maps corresponding to the following anatomical regions: telencephalon, optic tectum, midbrain, cerebellum, whole brain, and skeletal muscle. Additionally, we defined ROIs over the neuroblastoma of the transgenic zebrafish.

2.6 | Histology

Immunohistochemistry was performed for intraorganismal orientation and special distribution of tumors immediately after MRE (approx. 1 h after death) in 2 formaldehyde-fixed paraffin-embedded whole mount zebrafish. Tyrosine hydroxylase (TH) is an enzyme found

in adrenergic tissues; therefore, it can be used as marker confirming the identity of the tumor.⁴³ To improve distribution of the fixative inside the tissue, 5 mm of the caudal fin was removed before the carcass was fixed in 4% paraformaldehyde in 1× phosphate buffered saline on a rocker for 48 h at 4°C. After fixation, paraformaldehyde was replaced by decalcification buffer (0.5 M EDTA, pH: 7.2), and fish were incubated on a rocker for 24 h at 4°C. The fish were paraffin-embedded and sectioned (12 μm) as described in Her et al.⁴⁴ Cancerous tissue was identified using a TH as well as hematoxylin and eosin staining. Prior to TH staining, sections were rehydrated with subsequent baths of 5 min each in xylene (2 times), 100% EtOH (2 times), and 70% EtOH. Sections were then rinsed in water and placed in TBS-T for 5 min. Slides were heated to approximately 90°C for 20 min in citrate buffer, incubated 1 h in blocking buffer and incubated overnight with primary antibody (anti-TH: Pel-Freeze, cat # P40101-150) at a dilution of 1:200. The next day, slides were rinsed with TBS-T and incubated for 1 h with secondary antibody (goat anti-rabbit IgG H&L, conjugated with Alexa 488 (abcam, cat# ab150077) at 1:500. Glass slides were mounted using an antifade mounting agent (ProLong Gold Antifade Mounting Agent, Invitrogen; cat# P36935) to seal and preserve the fluorescently labeled tissue. For hematoxylin and eosin staining, which stains nuclei in dark purple and extracellular matrix in pink, the following protocol was used: formaldehyde-fixed paraffin-embedded fish were dewaxed 5 min in xylene, then again for 10 min in fresh xylene, 5 min in 100% EtOH, 2 min in 80% EtOH, 2 min in 70% EtOH, and 2 times in H₂O for 1 min. Next, the tissue was then stained with Mayer hematoxylin for 5 min and rinsed for 5 min in running tap water. Differentiation (10 dips in 0.3% acid alcohol) and blueing (20 dips in 95% EtOH) steps were performed, and formaldehyde-fixed paraffin-embedded tissue was then stained with Eosin-Phloxine solution for 2 min and dehydrated with subsequent baths of 5 min in 95% EtOH, 100% EtOH (2 times), and xylene (2 times). Slides were covered with mounting agent (Eukitt quick-hardening mounting agent, Sigma-Aldrich; cat# 03989) and mounted on glass slides.

2.7 | Statistical analysis

We tested the significance of population differences using the Wilcoxon rank sum test using MatLab 9.8.0.1380330 (R2020a) Update 2 (MathWorks, Natick, MA). Multiple comparisons were done using a 1-way analysis of variance in conjunction with the Bonferroni method. Therefore, we first defined 3 groups: wild type fish, tumor-bearing fish, and the pooled cohort of all fish. We then determined if region values in the brain were different between group

1 (wild type) and 2 (tumor). Because no difference was found, we further analyzed nontumor regions in the pooled group. In group 2 (tumor), we separately analyzed regional differences between tumor tissue, muscle tissue, and brain tissue. To test correlations between SWS or φ values and age or tumor size, we used the Pearson correlation. We did not test for sex effects on MRE parameters. p Values less than .05 were considered to indicate statistically significant differences. Unless otherwise indicated, the SD is used as an error estimation.

3 | RESULTS

3.1 | Phantom experiments

Comparison of inversion-based mapping at different resolutions with ground truth acquired by tabletop MRE in a wider frequency range and global Bessel fitting is presented in Figure 2. In Figure 2A, we show unfiltered wave images acquired in the gel phantom for each frequency and resolution. Wave fit analysis using Bessel functions resulted in a mean SWS of 0.77 ± 0.09 m/s and a mean φ of 0.30 ± 0.08 rad, which we considered ground truth. We then compared both ground truths with the results of our processing pipeline and found good agreement across all frequencies and resolutions, as shown in Figure 2B. Albeit phantom MRE values were unaffected by resolution, the SNR for $40 \times 40 \mu\text{m}^2$ was significantly lower than that obtained by larger voxel sizes ($p < .05$). Henceforth, we chose a resolution of $60 \times 60 \mu\text{m}^2$ for all animal experiments to ensure a stable range of SNR unaffected by resolution. Figure 2C shows the results of both the SWS recovered by Bessel fit as well as SWS recovered by our k-MDEV pipeline (both at $60 \times 60 \mu\text{m}^2$) compared to independent measurements of the same material at our 0.5 Telsa tabletop MRE system. At the relevant frequencies, the results fall closely together, validating our approach. A $60 \times 60 \mu\text{m}^2$ resolution provided SNRs of 19 ± 5 , 21 ± 4 , and 21 ± 4 for 1000, 1200, and 1400 Hz, respectively, which was close to the phantom SNR reported in Ref. 24 despite the higher resolution used in the present study.

3.2 | Zebrafish MRE

Group mean vibration amplitudes in the brains were $9 \pm 6 \mu\text{m}$ at 1000 Hz, $10 \pm 8 \mu\text{m}$ at 1200 Hz, and $12 \pm 6 \mu\text{m}$ at 1400 Hz. Mean displacement SNR averaged over all analyzed ROIs was 14 ± 7 , 16 ± 7 , and 19 ± 7 for 1000, 1200, and 1400 Hz, respectively, which is higher than reported in the literature based on single-shot MRE.²⁴ Coronal SWS and φ maps of a 1-year-old zebrafish are shown in

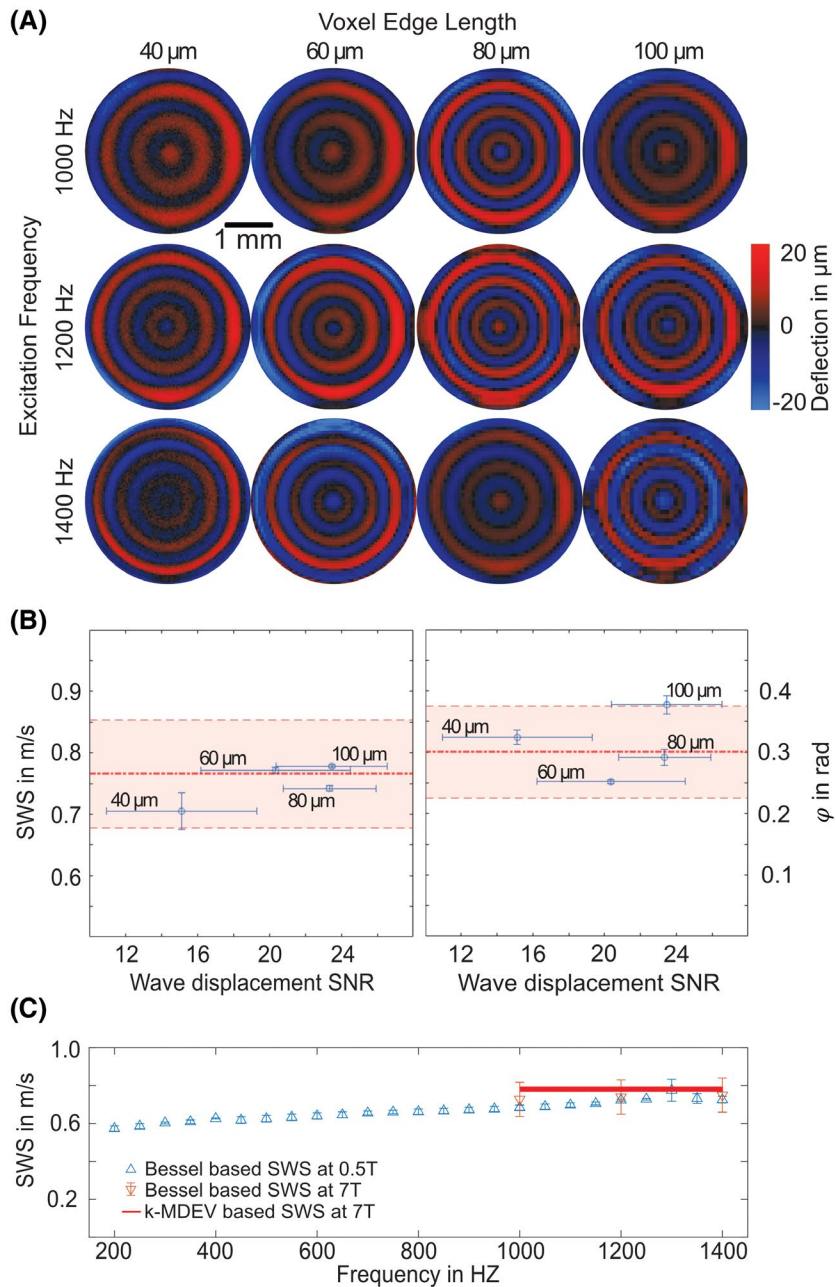


FIGURE 2 (A) Unfiltered wave images at different resolutions (columns) and frequencies (rows). (B) SWS (left) and ϕ (right) values determined by our processing pipeline plotted against wave displacement SNR. Bessel fits of the unfiltered complex-valued cylinder waves result in ground truths of $0.77 \text{ m/s} \pm 0.09 \text{ m/s}$ SWS and $0.30 \pm 0.08 \text{ rad}$ ϕ and are shown as dotted red line with SD as a shaded area. Both SWS values as well as ϕ determined by our pipeline fall within the ground truth for all resolutions. The percent error between the ground truth and the values at $60 \times 60 \mu\text{m}^2$ are 5% for the SWS and 10% for ϕ . (C) Comparison of tabletop MRE with 7T MRE both analyzed using frequency-resolved Bessel functions and frequency compounded k-MDEV inversion at $60 \times 60 \mu\text{m}^2$. Between 1000 and 1400 Hz, all measurements fall into the same SD range (thickness of the horizontal red line indicates SD). The percent error between the Bessel-based SWS at 7T and the k-MDEV based SWS was 5%, whereas the percent error between the Bessel-based SWS at 0.5T and the k-MDEV measurement was 9%. ϕ , loss angle; MDEV, multifrequency dual elastovisco; SWS, shear wave speed

Figure 3. Subregions of the brain, muscle, and tumor tissue can be identified in MRE maps, as indicated by the corresponding ROI boundaries, which are superimposed on the magnitude MRE images. To visualize the relative position of the MRE-slices, a composite microscopy image of a transgenic fish is shown overlaid with the approximate slice position, with green fluorescent protein marking the location of the tumor. Local, unphysical ϕ values greater than $\pi/2$ are most likely linked to inhomogeneities at tissue boundaries.⁴⁵

We observed no difference between brain regions of wild-type and tumor-bearing zebrafish. Henceforth, the results from both groups were pooled for group statistical analysis. SWS values were higher in the midbrain region

($3.1 \pm 0.7 \text{ m/s}$) than in the optic tectum ($2.6 \pm 0.5 \text{ m/s}$) and telencephalon ($2.6 \pm 0.5 \text{ m/s}$) ($p < .05$). ϕ values were lower in the cerebellum ($0.9 \pm 0.4 \text{ rad}$) than in the telencephalon ($1.4 \pm 0.2 \text{ rad}$) and optic tectum ($1.3 \pm 0.4 \text{ rad}$). We found no influence of age or tumor size on SWS or ϕ values in our fish using Pearson r ($p > .05$).

The sites of cancer cells identified by immunohistochemistry with TH antibody and hematoxylin and eosin staining agreed remarkably well with features visible in the SWS and ϕ maps, as shown in Figure 4. Comparing mean tumor values with muscle and brain tissue in the neuroblastoma-bearing fish, we found SWS and ϕ of cancerous tissue ($2.4 \pm 0.3 \text{ m/s}$, $0.7 \pm 0.1 \text{ rad}$) to be lower than those of skeletal muscle ($2.9 \pm 0.5 \text{ m/s}$, $1.4 \pm 0.2 \text{ rad}$)

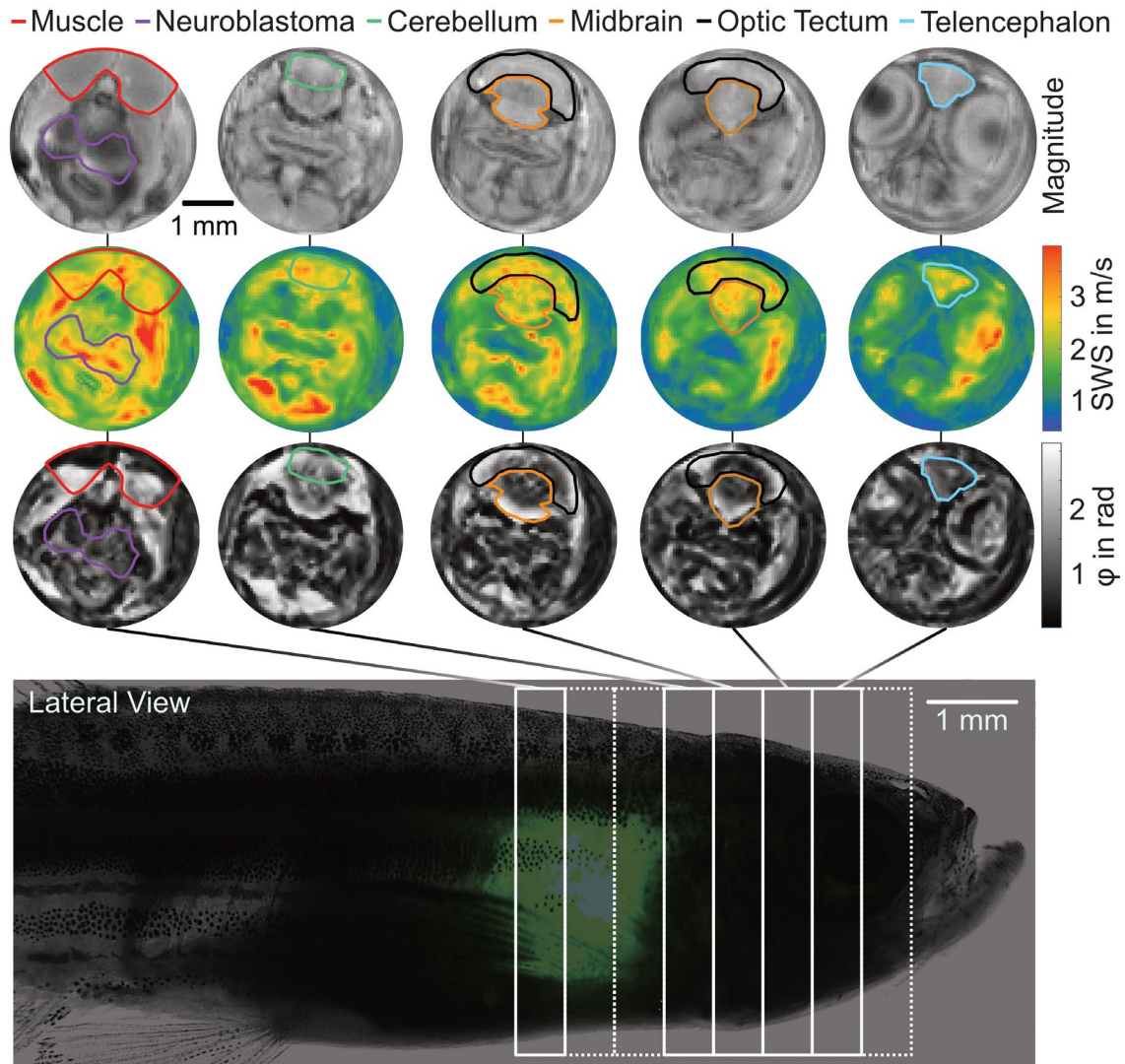


FIGURE 3 Representative data obtained in a transgenic zebrafish. The first row shows absolute wave magnitude maps, with coronal slices from posterior to anterior. SWS and ϕ maps of the respective slices are shown in the second and third rows, respectively. Anatomical regions relevant in our study are marked in all maps. The bottom row shows approximate slice positioning overlaid over a composite microscopy image of an anesthetized zebrafish that shows general anatomy, with GFP indicating the tumor through the semitransparent skin. GFP, green fluorescent protein

and brain tissue (2.9 ± 0.4 m/s, 1.2 ± 0.2 rad, all $p < .05$). Tumor volume based on multiple ROI was no confounder for SWS or loss angle. Group statistical data are plotted in Figure 5 and summarized in Table 1.

4 | DISCUSSION

To the best of our knowledge, this is the first study presenting spatially resolved maps of SWS and loss angle ϕ of the adult zebrafish. SWS is used in studies as a surrogate marker of stiffness.⁴⁶ Recently, SWS ranging from 2.5 to 5 m/s for frequencies of 300 to 500 Hz was found in anesthetized zebrafish, which is slightly above our results despite lower frequencies.¹⁴ However, the published values

do not account for the spatial heterogeneity of mechanical properties, as seen in our study, and reflect tissue properties in a central region of the fish not covered by our experiments.

Our results underline the great potential of MRE in generating viscoelasticity maps with a spatial resolution of 60 μm , which to our knowledge is the highest resolution thus far reported for MRE parameter mapping. This high resolution was particularly favorable for investigating the heterogeneity of zebrafish anatomy by MRE. An interesting finding of our study is that stiffness is higher in the mesencephalon region than in the optic tectum, which could point to microstructural differences. For example, the optic tectum is characterized by the presence of fewer though better aligned neuronal fibers, whereas

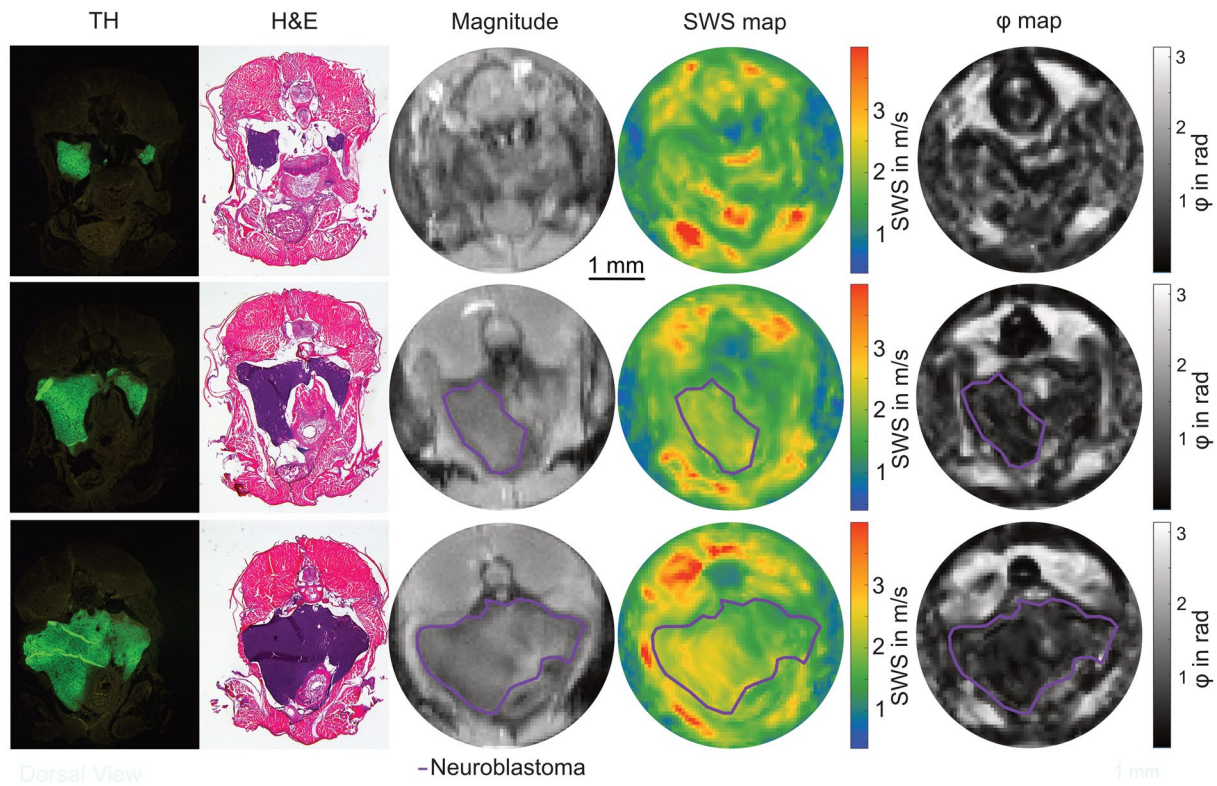


FIGURE 4 Comparison of SWS as well as ϕ maps and histology. TH and H&E staining reveal cancerous cells in green and purple, which can then be identified in the magnitude, SWS, and ϕ maps. Note the different thicknesses of the slices, with histology slices being significantly thinner ($<4 \mu\text{m}$) than MRE slices ($600 \mu\text{m}$). The cancerous region is marked in purple. H&E, hematoxylin and eosin; TH, tyrosine hydroxylase

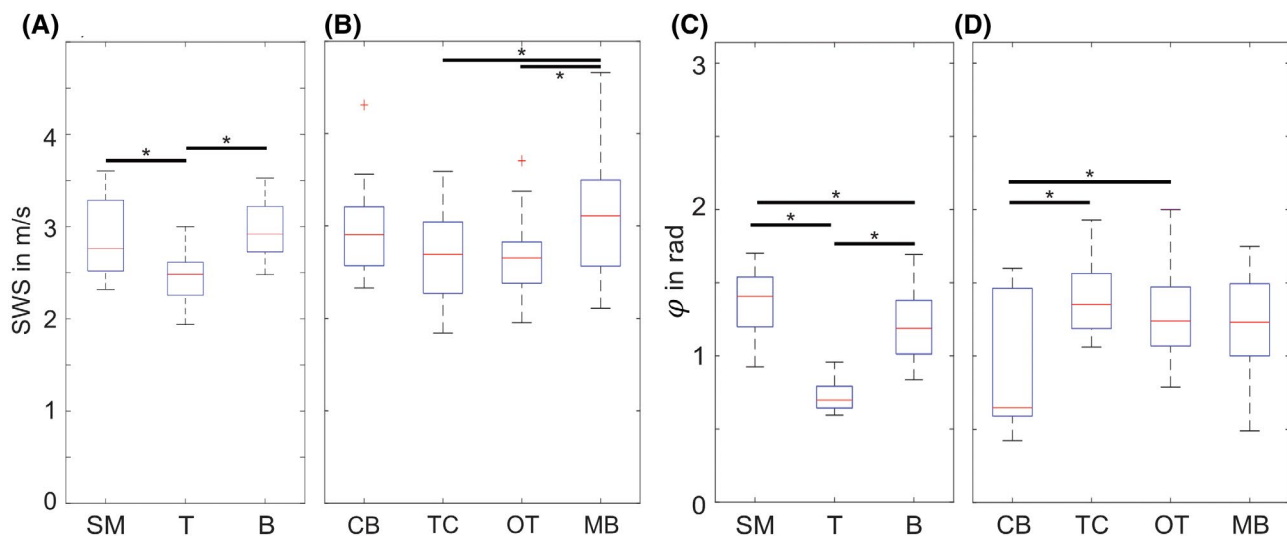


FIGURE 5 Group SWS (A,B) and loss angle values (C,D) for SM, T, B, CB, TC, OT, and MB. In (B) and (D), transgenic zebrafish and wild-type zebrafish were pooled, whereas (A) and (C) only show transgenic fish. Significant differences ($p < .05$) are indicated by asterisks. B, whole brain; CB, cerebellum; MB, midbrain; OT, optic tectum; SM, skeletal muscle; T, neuroblastoma; TC, telencephalon

the middle mesencephalon is dominated by distinct fibers and abundant fiber crossings, which might contribute to greater stiffness than in the optic tectum overall. Fish brain stiffness values seem to be similar to that of the murine brain as investigated by MRE in the same frequency

range,^{24,47–50} underscoring the viability of zebrafish as an animal model from a mechanical perspective. Another interesting finding of our experiments is that neuroblastoma tissue is markedly softer and less viscous than muscle and brain tissue. This suggests similar mechanical

TABLE 1 Shear wave speed loss angle and magnitude shear modulus of different tissue types in zebrafish

Region of Interest	SWS in m/s	ϕ in Rad	$ G^* $ in kPa
<i>Transgenic fish only</i>			
Whole brain	2.9 ± 0.4	1.2 ± 0.2	5.7 ± 0.2
Skeletal muscle	2.9 ± 0.5	1.4 ± 0.2	4.9 ± 0.2
Neuroblastoma	2.4 ± 0.3	0.7 ± 0.1	5.0 ± 0.1
<i>All fish</i>			
Telencephalon	2.6 ± 0.5	1.4 ± 0.2	3.9 ± 0.3
Optic tectum	2.6 ± 0.5	1.3 ± 0.4	4.3 ± 0.2
Midbrain	3.1 ± 0.7	1.2 ± 0.3	6.5 ± 0.5
Cerebellum	2.9 ± 0.6	0.9 ± 0.4	6.8 ± 0.3

Note: Error is given as SD.

Abbreviations: ϕ , loss angle; G^* , shear modulus; Rad, radian; SWS, shear wave speed.

properties of our tumor model as observed in invasively growing human brain tumors such as glioblastoma, which are characterized by a relatively low amount of collagen.⁵¹ This might provide a unique window into the soft signature of malignant tumor cells, which is typically masked by stiff properties of fibrous proteins in other tumors.⁵²

Comparing our methodology with other biomechanical methods underscores its relevance. Brillouin microscopy has revealed interesting details of mechanical phenomena during growth and repair of the spinal cord in zebrafish larvae with a microscopic resolution of up to 7 μm but cannot measure shear modulus.⁵³ Direct contact setups such as biocompatible cantilevers are able to measure mean total strain during the embryo stage and can be combined with finite-element analysis to estimate spatially resolved Young modulus, but they are invasive and rely on model assumptions.⁵⁴ Similarly, optical traps can be used to measure pointwise stiffness values.^{55,56} However, because this method is based on the deflecting responses off transparent beads, the invasive injection of foreign material is necessary, which might also change the elastic properties of the tissue. Another powerful method is scanning atomic force microscopy,⁵⁷ which, however, needs thin tissue slices and careful surface preparation, hindering its direct comparison with bulk parameters measured by MRE. Additionally, many methods exist to measure specific mechanical properties of individual parts of the fish, such as caudal fins,⁵⁸ heart sections,⁸ or neuromasts,⁵⁹ but these methods cannot easily be applied to heterogeneous tissues within the fish body as investigated in our study.

More experiments are needed to address viscoelastic dispersion and region-specific differences beyond those addressed in this paper. Another limitation is the small

number of zebrafish and their uneven age distribution. Finally, further technical developments are necessary to make MRE applicable to in vivo zebrafish. Similar to Refs. [14] and [60]. MRE could be applied to anesthetized fish, which would greatly enhance the viability of the method in biomedical research. To further reduce acquisition time, frequencies could be acquired in a parallel fashion as proposed by Solanas et al.⁶¹ Nevertheless, this preliminary proof-of-concept study successfully adds the zebrafish to the group of disease models accessible by MRE and extends the resolution limit of multifrequency MRE to 60- μm voxel edge size.

5 | CONCLUSION

In summary, an MRE setup was developed for postmortem viscoelasticity mapping in zebrafish. High-resolution maps of SWS and loss angle were generated by multifrequency wave acquisition and inversion with an in-plane resolution of 60 μm . These maps revealed rich detail of viscoelastic heterogeneities across skeletal muscle tissue, brain, and a model neuroblastoma. Reference values of stiffness and viscosity were tabulated for brain subregions including the cerebellum, optic tectum, telencephalon, and mesencephalon. This study provides the basis for new applications of MRE in biomedical research using zebrafish disease models.


ACKNOWLEDGMENT

Open access funding enabled and organized by ProjektDEAL.

ORCID

Jakob Ernst Luis Jordan  <https://orcid.org/0000-0002-6081-7595>

Tom Meyer  <https://orcid.org/0000-0002-2171-6791>

Heiko Tzschätzsch  <https://orcid.org/0000-0001-9458-2221>

Anton Gauert  <https://orcid.org/0000-0002-3013-5374>

Helge Herthum  <https://orcid.org/0000-0001-6494-0833>

Leif Schröder  <https://orcid.org/0000-0003-4901-0325>

Jürgen Braun  <https://orcid.org/0000-0001-5183-7546>

Anja I. H. Hagemann  <https://orcid.org/0000-0001-5491-4607>

Ingolf Sack  <https://orcid.org/0000-0003-2460-1444>

Ingolf Sack  <https://orcid.org/0000-0003-2460-1444>

TWITTER

Ingolf Sack  @bioqic

REFERENCES

1. Kinth P, Mahesh G, Panwar Y. Mapping of zebrafish research: a global outlook. *Zebrafish*. 2013;10:510-517.

2. Varga M. The doctor of delayed publications: the remarkable life of George Streisinger (1927-1984). *Zebrafish*. 2018;15:314-319.
3. Hagemann AIH, Kurz J, Kauffeld S, et al. In-vivo analysis of formation and endocytosis of the Wnt/ β -Catenin signaling complex in zebrafish embryos. *J Cell Sci*. 2014;127:3970-3982.
4. Gauert A, Olk N, Pimentel-Gutierrez H, et al. In vivo model for drug-response prediction in patients with B-cell precursor acute lymphoblastic leukemia. *Cancers (Basel)*. 2020;12:1883.
5. Marques IJ, Lupi E, Mercader N. Model systems for regeneration: zebrafish. *Development*. 2019;146:18.
6. Lammer E, Carr GJ, Wendler K, Rawlings JM, Belanger SE, Braunbeck T. Is the fish embryo toxicity test (FET) with the zebrafish (*Danio rerio*) a potential alternative for the fish acute toxicity test? *Comp Biochem Physiol C Toxicol Pharmacol*. 2009;149:196-209.
7. Howe K, Clark MD, Torroja CF, et al. The zebrafish reference genome sequence and its relationship to the human genome. *Nature*. 2013;496:498-503.
8. Yu JK, Sarathchandra P, Chester A, Yacoub M, Brand T, Butcher JT. Cardiac regeneration following cryoinjury in the adult zebrafish targets a maturation-specific biomechanical remodeling program. *Sci Rep*. 2018;8:15661.
9. Xiao J, Glasgow E, Agarwal S. Zebrafish xenografts for drug discovery and personalized medicine. *Trends Cancer*. 2020;6:569-579.
10. Spanjaard B, Hu B, Mitic N, et al. Simultaneous lineage tracing and cell-type identification using CRISPR-Cas9-induced genetic scars. *Nat Biotechnol*. 2018;36:469-473.
11. Holler K, Junker JP. RNA tomography for spatially resolved transcriptomics (Tomo-seq). In: Pelegri FJ, ed. *Vertebrate Embryogenesis: Embryological, Cellular, and Genetic Methods*. 2nd ed. Humana Press; 2019: 129-141.
12. Träber N, Uhlmann K, Girardo S, et al. Polyacrylamide bead sensors for in vivo quantification of cell-scale stress in zebrafish development. *Sci Rep*. 2019;9:17031.
13. Hörner F, Meissner R, Polali S, et al. Holographic optical tweezers-based in vivo manipulations in zebrafish embryos. *J Biophotonics*. 2017;10:1492-1501.
14. Zhang XM, Zhang AX, Zhou BR, Xu XL. A feasibility study for noninvasive measurement of shear wave speed in live zebrafish. *Ultrasonics*. 2020;107:106170.
15. Muthupillai R, Ehman RL. Magnetic resonance elastography. *Nature Med*. 1996;2:601-603.
16. Hirsch S, Braun J, Sack I. *Magnetic Resonance Elastography: Physical Background and Medical Applications*. Wiley-VCH; 2017.
17. Majumdar S, Klatt D. Longitudinal study of sub-regional cerebral viscoelastic properties of 5XFAD Alzheimer's disease mice using multifrequency MR elastography. *Magn Reson Med*. 2021;86:405-414.
18. Liu Y, Royston TJ, Klatt D, Lewandowski ED. Cardiac MR elastography of the mouse: initial results. *Magn Reson Med*. 2016;76:1879-1886.
19. Pagé G, Tardieu M, Gennisson JL, Besret L, Garteiser P, Van Beers BE. Tumor solid stress: assessment with MR elastography under compression of patient-derived hepatocellular carcinomas and cholangiocarcinomas xenografted in mice. *Cancers (Basel)*. 2021;13:1891.
20. Li J, Zormpas-Petridis K, Boulton JKR, et al. Investigating the contribution of collagen to the tumor biomechanical phenotype with noninvasive magnetic resonance elastography. *Cancer Res*. 2019;79:5874-5883.
21. Guertler CA, Okamoto RJ, Schmidt JL, Badachhapa AA, Johnson CL, Bayly PV. Mechanical properties of porcine brain tissue in vivo and ex vivo estimated by MR elastography. *J Biomech*. 2018;69:10-18.
22. Feng Y, Clayton EH, Chang Y, Okamoto RJ, Bayly PV. Viscoelastic properties of the ferret brain measured in vivo at multiple frequencies by magnetic resonance elastography. *J Biomech*. 2013;46:863-870.
23. Bertalan G, Klein C, Schreyer S, et al. Biomechanical properties of the hypoxic and dying brain quantified by magnetic resonance elastography. *Acta Biomater*. 2020;101:395-402.
24. Bertalan G, Guo J, Tzschätzsch H, et al. Fast tomoelastography of the mouse brain by multifrequency single-shot MR elastography. *Magn Reson Med*. 2019;81:2676-2687.
25. Guo J, Bertalan G, Meierhofer D, et al. Brain maturation is associated with increasing tissue stiffness and decreasing tissue fluidity. *Acta Biomater*. 2019;99:433-442.
26. Ronot M, Lambert SA, Wagner M, et al. Viscoelastic parameters for quantifying liver fibrosis: three-dimensional multifrequency MR elastography study on thin liver rat slices. *PLoS One*. 2014;9:e94679.
27. Zhu B, Wei L, Rotile N, et al. Combined magnetic resonance elastography and collagen molecular magnetic resonance imaging accurately stage liver fibrosis in a rat model. *Hepatology*. 2017;65:1015-1025.
28. Othman SF, Xu H, Royston TJ, Magin RL. Microscopic magnetic resonance elastography (microMRE). *Magn Reson Med*. 2005;54:605-615.
29. Papazoglou S, Hirsch S, Braun J, Sack I. Multifrequency inversion in magnetic resonance elastography. *Phys Med Biol*. 2012;57:2329-2346.
30. Tzschätzsch H, Guo J, Dittmann F, et al. Tomoelastography by multifrequency wave number recovery from time-harmonic propagating shear waves. *Med Image Anal*. 2016;30:1-10.
31. Tao T, Sondalle SB, Shi H, et al. The pre-rRNA processing factor DEF is rate limiting for the pathogenesis of MYCN-driven neuroblastoma. *Oncogene*. 2017;36:3852-3867.
32. Braun J, Tzschätzsch H, Korting C, et al. A compact 0.5 T MR elastography device and its application for studying viscoelasticity changes in biological tissues during progressive formalin fixation. *Magn Reson Med*. 2018;79:470-478.
33. Zampini MA, Guidetti M, Royston TJ, Klatt D. Measuring viscoelastic parameters in Magnetic Resonance Elastography: a comparison at high and low magnetic field intensity. *J Mech Behav Biomed Mater*. 2021;120:104587.
34. Sauer F, Oswald L, Ariza de Schellenberger A, et al. Collagen networks determine viscoelastic properties of connective tissues yet do not hinder diffusion of the aqueous solvent. *Soft Matter*. 2019;15:3055-3064.
35. Wallace CK, Bright LA, Marx JO, Andersen RP, Mullins MC, Carty AJ. Effectiveness of rapid cooling as a method of euthanasia for young zebrafish (*Danio rerio*). *J Am Assoc Lab Anim Sci*. 2018;57:58-63.
36. Li M, Guo J, Hu P, et al. Tomoelastography based on multifrequency MR elastography for prostate cancer detection: comparison with multiparametric MRI. *Radiology*. 2021;299:201852.
37. Herthum H, Shahryari M, Tzschätzsch H, et al. Real-time multifrequency MR elastography of the human brain reveals rapid

- changes in viscoelasticity in response to the Valsalva Maneuver. *Front Bioeng Biotechnol.* 2021;9:666456.
38. Mura J, Schrank F, Sack I. An analytical solution to the dispersion-by-inversion problem in magnetic resonance elastography. *Magn Reson Med.* 2020;84:61-71.
 39. Okamoto RJ, Clayton EH, Bayly PV. Viscoelastic properties of soft gels: comparison of magnetic resonance elastography and dynamic shear testing in the shear wave regime. *Phys Med Biol.* 2011;56:6379-6400.
 40. Donoho DL, Johnstone IM, Kerkycharian G, Picard D. Wavelet shrinkage: asymptopia? *J R Stat Soc Series B-Methodol.* 1995;57:301-337.
 41. Abdelnour AF, Selesnick IW. Nearly symmetric orthogonal wavelet bases. In *Proceedings of the IEEE International Conference on Acoustics, Speech, & Signal Processing (ICASSP)*, Salt Lake City, UT, May 2001.
 42. Barnhill E, Hollis L, Sack I, et al. Nonlinear multiscale regularisation in MR elastography: towards fine feature mapping. *Med Image Anal.* 2017;35:133-145.
 43. Reynolds CP, Biedler JL, Spengler BA, et al. Characterization of human neuroblastoma cell lines established before and after therapy. *J Natl Cancer Inst.* 1986;76:375-387.
 44. Her ZP, Yeo KS, Howe C, Levee T, Zhu S. Zebrafish model of neuroblastoma metastasis. *J Vis Exp.* 2021. doi:10.3791/62416
 45. Dittmann F, Hirsch S, Tzschatzsch H, Guo J, Braun J, Sack I. In vivo wideband multifrequency MR elastography of the human brain and liver. *Magn Reson Med.* 2016;76:1116-1126.
 46. Manduca A, Bayly PJ, Ehman RL, et al. MR elastography: principles, guidelines, and terminology. *Magn Reson Med.* 2021;85:2377-2390.
 47. Clayton EH, Garbow JR, Bayly PV. Frequency-dependent viscoelastic parameters of mouse brain tissue estimated by MR elastography. *Phys Med Biol.* 2011;56:2391-2406.
 48. Boulet T, Kelso ML, Othman SF. Long-term in vivo imaging of viscoelastic properties of the mouse brain after controlled cortical impact. *J Neurotrauma.* 2013;30:1512-1520.
 49. Schregel K, Wuerfel E, Garteiser P, et al. Demyelination reduces brain parenchymal stiffness quantified in vivo by magnetic resonance elastography. *Proc Natl Acad Sci U S A.* 2012;109:6650-6655.
 50. Jamin Y, Boulton JK, Li J, et al. Exploring the biomechanical properties of brain malignancies and their pathologic determinants in vivo with magnetic resonance elastography. *Cancer Res.* 2015;75:1216-1224.
 51. Streitberger KJ, Lilaj L, Schrank F, et al. How tissue fluidity influences brain tumor progression. *Proc Natl Acad Sci U S A.* 2020;117:128-134.
 52. Plodinec M, Loparic M, Monnier CA, et al. The nanomechanical signature of breast cancer. *Nat Nanotechnol.* 2012;7:757-765.
 53. Schlusser R, Mollmert S, Abuhattum S, et al. Mechanical mapping of spinal cord growth and repair in living zebrafish larvae by Brillouin imaging. *Biophys J.* 2018;115:911-923.
 54. Tomizawa Y, Dixit K, Daggett D, Hoshino K. Biocompatible cantilevers for mechanical characterization of zebrafish embryos using image analysis. *Sensors (Basel).* 2019;19:1506.
 55. Staunton JR, Blehm B, Devine A, Tanner K. In situ calibration of position detection in an optical trap for active microrheology in viscous materials. *Opt Express.* 2017;25:1746-1761.
 56. Blehm BH, Devine A, Staunton JR, Tanner K. In vivo tissue has non-linear rheological behavior distinct from 3D biomimetic hydrogels, as determined by AMOTIV microscopy. *Biomaterials.* 2016;83:66-78.
 57. Möllmert S, Kharlamova MA, Hoche T, et al. Zebrafish spinal cord repair is accompanied by transient tissue stiffening. *Biophys J.* 2020;118:448-463.
 58. Puri S, Aegerter-Wilmsen T, Jaźwińska A, Aegerter CM. In vivo quantification of mechanical properties of caudal fins in adult zebrafish. *J Exp Biol.* 2018;221:jeb171777.
 59. McHenry MJ, van Netten SM. The flexural stiffness of superficial neuromasts in the zebrafish (*Danio rerio*) lateral line. *J Exp Biol.* 2007;210:4244-4253.
 60. Kabli S, Spaink HP, De Groot HJ, Alia A. In vivo metabolite profile of adult zebrafish brain obtained by high-resolution localized magnetic resonance spectroscopy. *J Magn Reson Imaging.* 2009;29:275-281.
 61. Sango Solanas P, Tse Ve Koon K, Ratiney H, Millioz F, Caussy C, Beuf O. Harmonic wideband simultaneous dual-frequency MR Elastography. *NMR Biomed.* 2021;34:e4442.

How to cite this article: Jordan JEL, Bertalan G, Meyer T, et al. Microscopic multifrequency MR elastography for mapping viscoelasticity in zebrafish. *Magn Reson Med.* 2022;87:1435-1445. doi:[10.1002/mrm.29066](https://doi.org/10.1002/mrm.29066)